frontiers | Frontiers in Physics

ORIGINAL RESEARCH
published: 18 July 2022
doi: 10.3389/fphy.2022.933285

Ultraprecise Off-Axis Atom Localization With Hybrid Fields

*Ning Jia[1], Xing-Dong Zhao[2], Wen-Rong Qi[2] and Jing Qian[3]**

[1]*Public Experiment Center, University of Shanghai for Science and Technology, Shanghai, China,* [2]*School of Physics, Henan Normal University, Xinxiang, China,* [3]*State Key Laboratory of Precision Spectroscopy, Department of Physics, Quantum Institute for Light and Atoms, School of Physics and Electronic Science, East China Normal University, Shanghai, China*

Atom localization enables a high-precision imaging of the atomic position, which has provided vast applications in fundamental and applied science. In the present work, we propose a scheme for realizing two-dimensional off-axis atom localization in a three-level Λ system. Benefiting from the use of a hybrid coupling field, which consists of one Gaussian beam and one Laguerre–Gaussian beam, our scheme shows that the atoms can be localized at arbitrary position with high spatial resolution. Considering realistic experimental parameters, our numerical simulation predicts that the atoms can be precisely localized with a spatial resolution of ~ 200 nm in the range of a radial distance of a few micrometers to the beam core. Our results provide a more flexible way to localize atoms in a two-dimensional system, possibly paving one-step closer to the nanometer scale atom lithography and ultraprecise microscopy.

Keywords: off-axis localization, Laguerre–Gaussian beam, ultraprecise, quantum interference, three-level atom

OPEN ACCESS

Edited by:
Weibin Li,
University of Nottingham,
United Kingdom

Reviewed by:
Bernhard Johan Hoenders,
University of Groningen, Netherlands
Zhaoyang Zhang,
Xi'an Jiaotong University, China

****Correspondence:***
Jing Qian
jqian1982@gmail.com

Specialty section:
This article was submitted to Quantum Engineering and Technology, a section of the journal Frontiers in Physics

Received: *30 April 2022*
Accepted: *20 June 2022*
Published: *18 July 2022*

Citation:
Jia N, Zhao X-D, Qi W-R and Qian J (2022) Ultraprecise Off-Axis Atom Localization With Hybrid Fields. Front. Phys. 10:933285. doi: 10.3389/fphy.2022.933285

1 INTRODUCTION

Nowadays, the Laguerre–Gaussian (LG) beam [1] has engendered tremendous advanced applications [2–7]. For example, it is widely used in the superresolution fluorescence microscopy such as the stimulated emission depletion [8, 9] and minimal photon fluxes [10, 11] in order to overcome the diffraction limit. Another approach to this target is utilizing the spatially dependent coherent light–matter interaction in atom-light coupling systems [12–14], which essentially depends on a spatially modulated atom-light coupling. By the detection of spontaneously emitted photons [15–18], level population [19–25], absorption [26–28], and gain [29, 30], subwavelength-scale atom localization can be obtained.

As far as we know, atom localization with LG beams can exhibit a large number of advantages [31, 32]. For example, the LG beam has a donut intensity spot naturally, which may avoid the need of two orthogonal standing wave (SW) fields for generating spatially modulated atom-light coupling in a two-dimensional (2D) atom localization system. That fact largely reduces the complexity of experimental implementation. Moreover, it is easier to create a single excitation spot in its core by a LG beam. In traditional SW-based localization schemes, due to the periodicity of the SW field intensity there may exist more than one localization spots within single optical wavelength. Therefore after one-time measurement, the probability of finding atoms at a certain position can be deeply reduced. So far, some approaches have been proposed to break this periodicity of SW fields, *via* utilizing the sensitivity of light–matter interactions to the light phase in a closed-loop atomic system [33, 34] and the interference of multiple SW fields with different wavelengths and phases [35, 36]. These methods, however, will increase the complexity of experimental setup. Although the LG beam has the aforementioned advantages in localization, it can only localize atoms in the vicinity of its beam core where the laser intensity is close to zero. Off-axis atom localization must be accompanied by the movement of the LG beam itself, which undoubtedly adds to extra complexity.

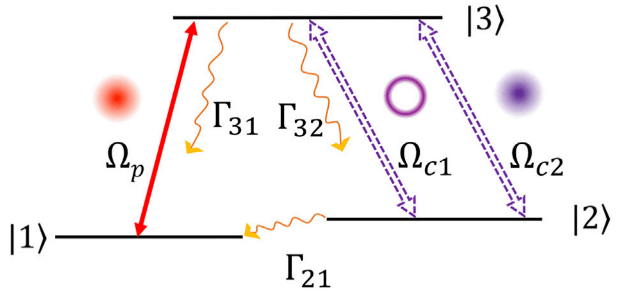

FIGURE 1 | Schematic of a Λ-type three-level system where the probe field Ω_p for the transition of states $|1\rangle$ and $|3\rangle$ is a Gaussian beam. The coupling field between $|3\rangle$ and $|2\rangle$ is composed by one LG beam Ω_{c1} and one Gaussian beam Ω_{c2}. Γ_{nm} denotes the spontaneous decay rates from $|n\rangle$ to $|m\rangle$.

In traditional SW localization schemes, the superposition of multiple SW lasers with different wavelengths and phases is commonly adopted for reaching a single excitation point [35, 36]. In addition this effect between two LG beams can show interesting patterns such as optical Ferris wheels where the light intensity can be modulated to be zero in certain positions [37]. Inspired by these contributions, in the present work, we study a 2D off-axis atom localization in a three-level Λ system, in which a Gaussian beam serves as the probe field and a LG beam together with a Gaussian beam as the hybrid coupling field. The quantum interference effect between these two beams (LG and Gaussian) can achieve a unique zero-intensity spot at arbitrary position. We show that by appropriately tuning the ratio of peak amplitudes between the LG and any Gaussian beams, atoms can be localized at arbitrary position, with a certain distance to the beam core. Both the spatial resolution and radial distance of localization can be flexibly manipulated *via* tuning laser Rabi frequencies. Depending on the numerical simulation with experimental parameters our scheme enables the realization of an efficient off-axis 2D atom localization, accompanied by a best spatial resolution ~ 200 nm and a radial distance of a few micrometers. Our scheme provides a more convenient route to the target of ultraprecise off-axis 2D atom localization.

2 THEORETICAL STRATEGY

To describe the scheme mechanism we consider a simple three-level Λ system as displayed in **Figure 1**, where states $|1\rangle$ and $|3\rangle$ are resonantly coupled by a weak probe field Ω_p and states $|3\rangle$ and $|2\rangle$ are connected by another coupling field Ω_{c2}, with zero detuning. In order to realize an off-axis atom excitation, we have assumed that the probe and coupling beams as Gaussian beams, which are

$$\Omega_i(r) = \Omega_{i0} e^{-\frac{r^2}{W_i^2}}, \tag{1}$$

where $i = p$, $c2$ and Ω_{i0} represent the peak amplitude and W_i the Gaussian spot size. Remarkably, states $|3\rangle$ and $|2\rangle$ are also coupled by a second LG field Ω_{c1} at the same time, as [38].

$$\Omega_{c1}(r,\theta) = \Omega_{c10}\left(\frac{r}{W_{c1}}\right)^{|l|} e^{-\frac{r^2}{W_{c1}^2}} e^{il(\theta+\theta_{c1})}, \tag{2}$$

where Ω_{c10}, W_{c1}, θ_{c1}, and l are the peak amplitude, the beam waist, the initial phase, and the winding number, respectively. r and θ are the cylindrical radius and the azimuthal angle, respectively. Here, we take the winding number $l = 1$, which enables a single-spot excitation. Other higher-order modes with $l > 1$ would lower the localization precision by redistributing the atomic population among multiple azimuthal nodes. To our knowledge, this three-level model can be experimentally realized by the D1 line of ultracold ^{87}Rb atoms with energy levels $|1\rangle = |5S_{1/2}, F = 1\rangle$, $|2\rangle = |5S_{1/2}, F = 2\rangle$, and $|3\rangle = |5P_{1/2}, F = 2\rangle$. Based on Ref. [14], we assume the decay rates from $|3\rangle \to |1\rangle$ and $|3\rangle \to |2\rangle$ are equal, typically calculated by $\Gamma_{31} = \Gamma_{32} = 2\pi \times 5.75$ MHz. The decay rate between two hyperfine ground states $|1\rangle$ and $|2\rangle$ is $\Gamma_{21} = 5$ kHz, satisfying $\Gamma_{21} \ll \Gamma_{31}, \Gamma_{32}$ [39] so the lifetime of $|2\rangle$ is about 200μs. The beam width is $W_i = W_{c1} = W$ estimated to be same for simplicity. Under the frozen-gas limit where the atomic center of mass is unvaried we can take a measurement for the population on state $|2\rangle$ by collecting its fluorescence signals with a CCD camera and a well-localized position distribution of atoms could facilitate this measurement [14].

Considering a frozen atomic gas the time evolution of the systematic density-matrix elements can be described by ($\hbar = 1$) [40].

$$\begin{aligned}
\dot{\rho}_{11} &= \Gamma_{31}\rho_{33} + \Gamma_{21}\rho_{22} - i\Omega_p(\rho_{31} - \rho_{13}),\\
\dot{\rho}_{33} &= -(\Gamma_{31} + \Gamma_{32})\rho_{33} - i\Omega_p(\rho_{13} - \rho_{31}) - i\Omega_c(\rho_{23} - \rho_{32}),\\
\dot{\rho}_{12} &= -\gamma_{12}\rho_{12} - i\Omega_p\rho_{32} + i\Omega_c\rho_{13},\\
\dot{\rho}_{13} &= -\gamma_{13}\rho_{13} - i\Omega_p(\rho_{33} - \rho_{11}) + i\Omega_c\rho_{12},\\
\dot{\rho}_{23} &= -\gamma_{23}\rho_{23} + i\Omega_p\rho_{21} - i\Omega_c(\rho_{33} - \rho_{22}),
\end{aligned} \tag{3}$$

where $\rho_{nm} = \rho_{mn}^{\star}$ and $\sum_{n=1}^{3}\rho_{nn} = 1$ mean the conservation. The population on state $|2\rangle$ is solved by $\rho_{22} = 1 - \rho_{11} - \rho_{33}$. In deriving **Eq. 3** we have defined

$$\Omega_c = \Omega_{c1} + \Omega_{c2}, \tag{4}$$

representing the superposition of two coupling fields. Γ_{nm} denotes the spontaneous decay from $|n\rangle$ to $|m\rangle$ and γ_{nm} is defined as

$$\gamma_{12} = \Gamma_{21}/2, \gamma_{13} = (\Gamma_{31} + \Gamma_{32})/2, \gamma_{23} = (\Gamma_{32} + \Gamma_{31} + \Gamma_{21})/2. \tag{5}$$

The steady solutions of **Eq. 3** can be obtained by assuming $\dot{\rho}_{nm} = \dot{\rho}_{nn} = 0$. Due to the presence of decay Γ_{21}, it is intuitive that ρ_{22} decreases with Γ_{21}. Luckily, accounting for the condition of $\Gamma_{21} \ll \Gamma_{31(32)}$ that makes the effect of Γ_{21} negligible [23, 39], then ρ_{22} takes a simple form of

$$\rho_{22}(r,\theta) = \frac{1}{1 + I_c(r,\theta)/I_p(r)}, \tag{6}$$

where $\Gamma_{31} = \Gamma_{32}$, $\Gamma_{21} = 0$ are used. $I_c = |\Omega_{c1} + \Omega_{c2}|^2$ and $I_p = |\Omega_p|^2$ stand for the laser intensities. Note that $\rho_{22}(r,\theta)$ reveals a position-dependent feature due to the use of several structured fields. From **Eq. 6**, it is apparent that the condition $I_c(r_{loc}, \theta) \ll I_p(r_{loc})$ will cause $\rho_{22} \to 1$, which means a perfect atomic confinement can be achieved at arbitrary position r_{loc} in our scheme.

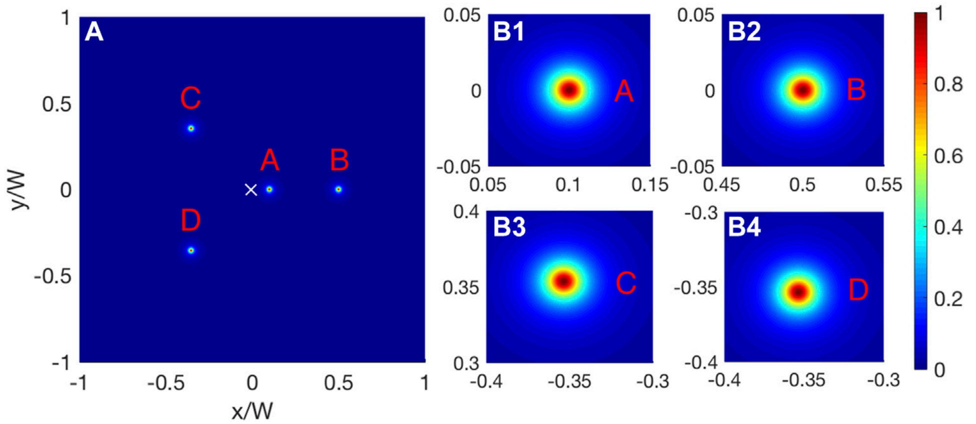

FIGURE 2 | Off-axis atom localization. **(A)** Off-axis localized positions A, B, C, and D with respect to $(\kappa_c, \theta_{c1}) = (0.1, \pi), (0.5, \pi), (0.5, \pi/4), (0.5, -\pi/4)$. The white cross denotes the center of light beams. **(B1–B4)** show the amplified images for the localized atomic positions, which have an off-axis feature. Here, $\Omega_{p0}/\Omega_{c10} = 0.01$.

3 OFF-AXIS LOCALIZATION

According to **Eq. 4** together with the definitions in **Eqs 1**, **2**, the intensity of the hybrid coupling field can be written as

$$I_c(r,\theta) = |\Omega_{c1} + \Omega_{c2}|^2 = \frac{\Omega_{c10}}{W^2} e^{-\frac{2r^2}{W^2}} \left| r + \kappa_c W e^{-i(\theta+\theta_{c1})} \right|^2, \quad (7)$$

where the peak ratio is $\kappa_c = \Omega_{c20}/\Omega_{c10}$, which can be tuned by Ω_{c20} if Ω_{c10} is fixed. Note that this hybrid coupling field is composed by one LG beam and one Gaussian beam, which resonantly couple states $|2\rangle$ and $|3\rangle$ at the same time. Finally we can arrive at an analytical solution to the equation $I_c(r, \theta) = 0$, that is, the perfect condition of localization can be reached at

$$(r_{loc}, \theta_{loc}) = (\kappa_c W, \pi - \theta_{c1}), \quad (8)$$

where the population ρ_{22} attains 1.0 in principle. That means atoms can be precisely placed at any desired position (r_{loc}, θ_{loc}) with a very high probability. While in fact, owing to the influence from intrinsic noises in the experimental setup, the observed localization resolution is quite limited. In **Section 5** we will discuss the fluctuation of laser intensities, the steady time as well as the noise from atomic thermal motion, in order to present a practical estimation for the experimental observation. Moreover, we have to point out that benefiting from the interference between two hybrid coupling fields Ω_{c1} and Ω_{c2} [41], the localization position (r_{loc}, θ_{loc}) can be widely adjusted by the beam parameters, which is not restricted merely at the beam core as in most previous works [31, 32].

As illustrated in **Figure 2A**, we show that atoms denoted as the steady population ρ_{22} on state $|2\rangle$, can be confined in any spatial position (r_{loc}, θ_{loc}) by changing the parameters (κ_c, θ_{c1}). For example when $(\kappa_c, \theta_{c1}) = (0.1, \pi), (0.5, \pi), (0.5, \pi/4), (0.5, -\pi/4)$, **Figure 2A** explicitly shows the off-axis atom localization at different positions as labeled by A ~D. **Figures 2B1–B4** amplify the distribution of atoms at different localized places. It is apparent that the spatial resolution of atom localization remains unchanged for different κ_c and θ_{c1}. Therefore, thanks to the zero-intensity point $(I_c(r, \theta) = 0)$ created by the interference between two light beams Ω_{c10} and Ω_{c20}, our scheme can realize an effective off-axis localization at arbitrary position in a 2D space.

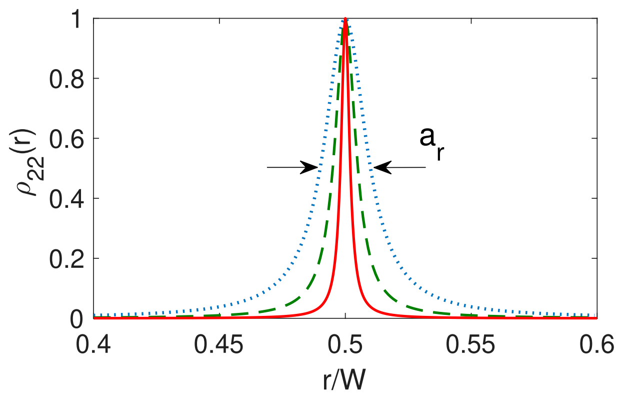

FIGURE 3 | Steady population distribution $\rho_{22}(r)$ along the radial direction r for $\kappa_p = \Omega_{p0}/\Omega_{c10} = 0.01$ (blue-dotted), 0.005 (green-dashed), and 0.002 (red-solid). a_r is the FWHM, which characterizes the spatial resolution of localization. Here, we use $\kappa_c = 0.5$.

4 ULTRAPRECISE LOCALIZATION

The quality of localization also depends on a high spatial resolution, which is characterized by the full width at half maximum (FWHM) of the steady distribution ρ_{22} (r, θ). A narrower linewidth indicates that the position of atoms can be well-resolved within a smaller range. By replacing the profiles of light fields (**Eqs 1**, **2**) the expression of $\rho_{22}(r)$ takes an explicitly Lorentz form

$$\rho_{22}(r) = \frac{1}{1 + \frac{(r - \kappa_c W)^2}{\kappa_p^2 W^2}}, \tag{9}$$

where we have omitted the azimuth angle by letting $\theta = \pi - \theta_{c1}$ and paid attention to the variation of $\rho_{22}(r)$ along the radial direction. We treat the FWHM of function $\rho_{22}(r)$ as a measurement to localization, which can also be analytically solved,

$$a_r = 2\kappa_p W. \tag{10}$$

In **Figure 3**, we plot the steady distribution $\rho_{22}(r)$ vs. r for different peak ratios κ_p. Clearly a weaker probe field leads to the atomic population more confined in the vicinity of the localization point $r = r_{loc} = 0.5W$, promising for a higher resolution localization. For example, we find that $a_r = 0.02W$ when $\kappa_p = 0.01$, but this value is decreased by one order of magnitude, which is $a_r = 0.004W$ as κ_p reduces to 0.002. From **Eq. 10**, it is intuitive that $a_r \to 0$ if $\kappa_p \ll 1$, enabling an ultraprecise localization under a sufficiently weak probe field. However in a realistic system, the fact that the time for a steady state becomes much longer in the weak probe limit, results in the atomic motion non-negligible. We will discuss this point in **Section 5.2**.

5 FEASIBILITY DISCUSSION

The numbers presented in this work are considered from ^{87}Rb where the lifetime of state $|3\rangle (= |5P_{1/2}, F = 2\rangle)$ is 27.7 ns [42], leading to the decay rates $\Gamma_{31} = \Gamma_{32} = 2\pi \times 5.75$ MHz, and the lifetime of $|2\rangle (= |5S_{1/2}, F = 2\rangle)$ is 200 μs, leading to $\Gamma_{21} = 5$ kHz. We assume that the co-propagating probe and coupling lasers are overlapping in space and have a same beam width $W = 5\,\mu m$. As explicitly presented in **section 3** and **section 4**, our scheme can achieve an ultraprecise off-axis atom localization due to the flexible manipulation of peak ratios κ_c and κ_p, together with the azimuth angle θ_{c1}. Due to the rotational invariance we ignore θ_{c1} by focusing on the radial distance r. However, as for an experimental implementation these parameters are also restrained. In this section, we numerically solve the spatial resolution a_r and the peak value of $\rho_{22}(r)$ by evolving the motional **Eq. 3** under more realistic conditions coming from measurement.

5.1 Laser Intensity Noise

To obtain realistic results evaluating experimental conditions, we introduce a perturbed laser intensity by adding a random intensity noise $\delta\Omega_i$ ($i = p$, $c1$, $c2$) to the peak value Ω_{i0} [43, 44]. The resulting fluctuated Rabi frequencies Ω_{i0}' can be written as

$$\Omega_{i0}' = \Omega_{i0} + \delta\Omega_i. \tag{11}$$

In the calculation, we assume $\delta\Omega_i/\Omega_{i0} \in [-\xi, \xi]$ and pay attention to the radial population distribution $\rho_{22}(r)$. During each measurement, the perturbation term $\delta\Omega_i$ can be a random number obtained from the range of $[-\xi, \xi]\Omega_{i0}$. By taking account of sufficient measurements, the average result can show the realistic observation in the experimental setup. Note that a larger Rabi frequency leads to stronger laser noise since $\delta\Omega_i \propto \Omega_{i0}$.

Figure 4 illustrates the distribution of steady population $\rho_{22}(r)$ under the influence of laser intensity noise, which is characterized by the factor ξ. By comparing **Figures 4A–D** it is apparent that a bigger ξ will give rise to a broadened population distribution with smaller peak values, which lowers the precision of localization. Furthermore, as for atoms localized closer to the beam core ($r = 0$) the intensity noise $\delta\Omega_{c2}$ [$\propto\Omega_{c20}$] is smaller due to $r_{loc} = \kappa_c W$. Therefore by positioning atoms far from the beam core the observation will suffer from a stronger laser intensity noise, in turn yielding a lower-quality localization, see **Figures 4A–D**. This fact gives a limitation to our protocol that the atoms cannot be placed very far from the beam core. A rough estimation (not shown) shows that the average peak value of $\rho_{22}(r)$ will be smaller than 0.2 if the radial localization distance r_{loc} is larger than 10 μm. In the experiment, a better control for the laser intensity noise can improve the scheme performance.

5.2 Time Needed for a Steady State

From **section 4**, we have known that ultraprecise localization with $a_r \to 0$ in principle relies on a sufficiently small κ_p, that is, $\Omega_{p0} \ll \Omega_{c10}$. This condition leads to the time T_s for reaching steady localization much longer. Because T_s is inversely proportional to the exact laser Rabi frequencies. For a longer T_s, the atomic thermal motion does play roles and the frozen-gas approximation fails. A discussion for the effect of atomic thermal motion can be seen in **section 5.3**. An efficient localization reports that T_s is so short to make the atomic movement during the steady time negligible. In the calculation, we consider atoms under the temperature $T = 1\,\mu K$ [14], with a most probable velocity $v_p = \sqrt{2k_B T/M} \approx 1.4$ cm/s, where k_B is the Boltzmann constant and M is the atomic mass. We introduce a new constraint to the resolution factor a_r

$$v_p T_s^{max} \le a_r \big/ 10, \tag{12}$$

where the real time T_s for a steady state should be smaller than $T_s^{\max}$ so as to make the atomic motion negligible during the measurement.

Figure 5 exhibits the steady time T_s as a function of the localization distance r_{loc} for different peak probe Rabi frequencies Ω_{p0}. Here, T_s is obtained by numerically evolving the master **Eq. 3**, considering all spontaneous decays. From **Figures 5A–D**, as decreasing Ω_{p0} we find that the steady time T_s (blue-solid) increases significantly; although the position of atoms can be well-resolved with a better spatial resolution (a_r becomes smaller) at the same time. According to the constraint (12), the maximal steady time $T_s^{\max}$ permitted for localization is labeled by the red-dashed line in the figure. When $T_s < T_s^{\max}$ atoms can obtain a robust localization. Obviously, in **Figures 5A,B** where the spatial resolution a_r is relatively large, atoms can be well localized within a wider radial range $r_{loc} < 5.3\,\mu m$ and $r_{loc} < 3.7\,\mu m$. Insets explicitly show the area of off-axis localization, which is denoted as a gray

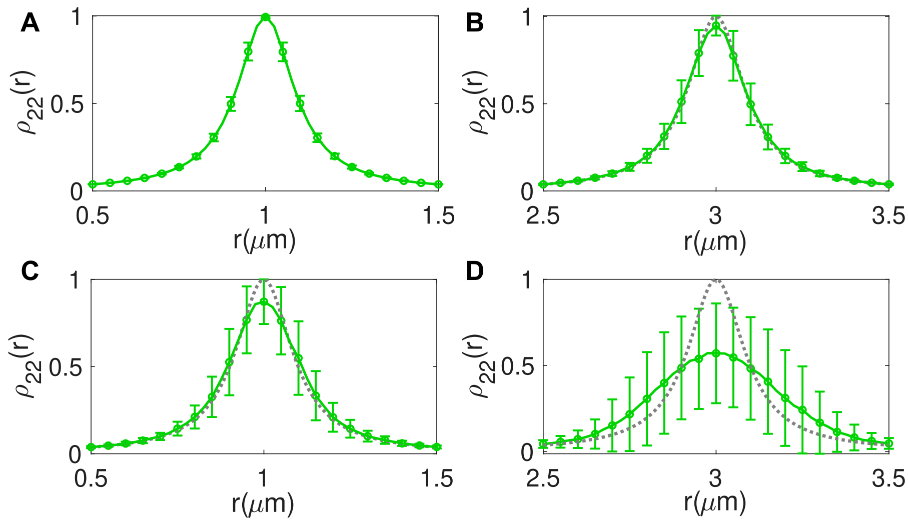

FIGURE 4 | Radial population distribution $\rho_{22}(r)$ under different intensity noises, which are given by **(A,B)** $\xi = 1.0\%$ and **(C,D)** $\xi = 5.0\%$ at different positions. We take 500 measurements for each point denoted by the error bar and the average result is shown by the green solid line. For comparison the black-dotted line indicates the result without any intensity noise, that is, $\xi = 0$. Here, $\Omega_{c20}/2\pi = (30, 90)$ MHz, respectively for **(A,C)** and **(B,D)**, corresponding to the localization positions $r_{loc} = (1.0, 3.0)\ \mu m$. Other parameters are $\Omega_{p0}/2\pi = 3$ MHz, $\Omega_{c10}/2\pi = 150$ MHz, and $W = 5\ \mu m$.

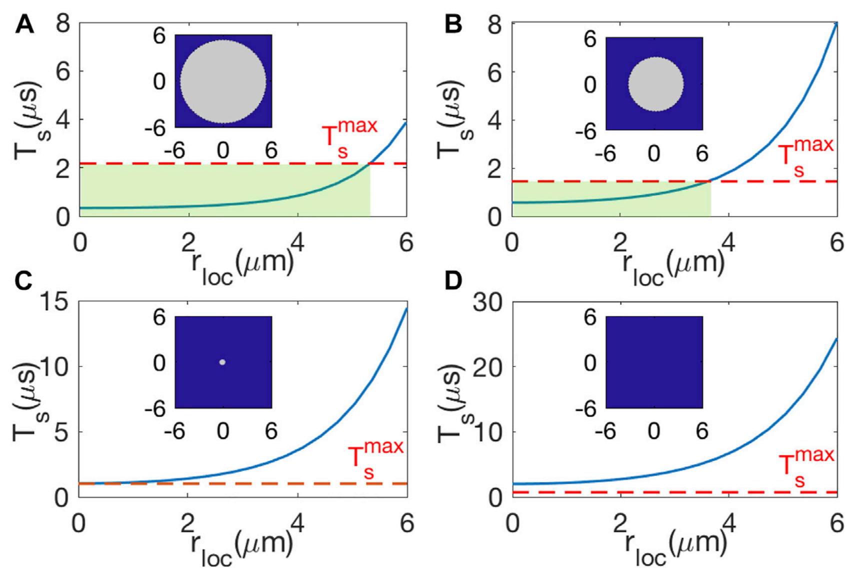

FIGURE 5 | Steady time T_s vs. the radius distance r_{loc} under **(A)** $\Omega_{p0}/2\pi = 4.5$ MHz and $a_r = 300$ nm, **(B)** $\Omega_{p0}/2\pi = 3.0$ MHz and $a_r = 200$ nm, **(C)** $\Omega_{p0}/2\pi = 2.1$ MHz and $a_r = 141$ nm, and **(D)** $\Omega_{p0}/2\pi = 1.5$ MHz and $a_r = 100$ nm. The red-dashed line denotes the maximal T_s permitted for an efficient localization. The shaded-green region stands for the radial range where atoms can be localized. Insets: effective off-axis localization is enabled within the gray disk. Here, $\Omega_{c10}/2\pi = 150$ MHz, $W = 5\ \mu m$, $\Omega_{c20} = r_{loc}\Omega_{c10}/W$, $T = 1\ \mu K$, and $\Gamma_{21} = 5$ kHz.

disk. In fact *via* an appropriate adjustment of κ_c and θ_{c1}, atoms can be confined at arbitrary position inside the gray disk.

Whereas, when Ω_{p0} is reduced to $2\pi \times 2.1$ MHz (**Figure 5C**), the reduction of a_r causes $T_s^{\max} \le T_s$ persistently. In this case only atom positioned at the beam core can be accurately confined so the protocol of off-axis localization fails. Furthermore, if $a_r <$ 141 nm, for example, $a_r = 100$ nm as in **Figure 5D**, the steady time T_s is maintained larger than the required $T_s^{\max}$, calculated by **Eq. 12** so no atoms could be localized. Because during such a longer steady time T_s most atoms have been moved away from the localization spot caused by their thermal motions, leading to a poor resolution (also see the discussion in **section 5.3**). Therefore, based on our analysis, we treat $a_r = 141$ nm as the best spatial resolution yet atoms can only be localized at the beam core. Effective off-axis localization needs to be at the expense of the spatial resolution. For example, a resolution of $a_r = 200$ nm

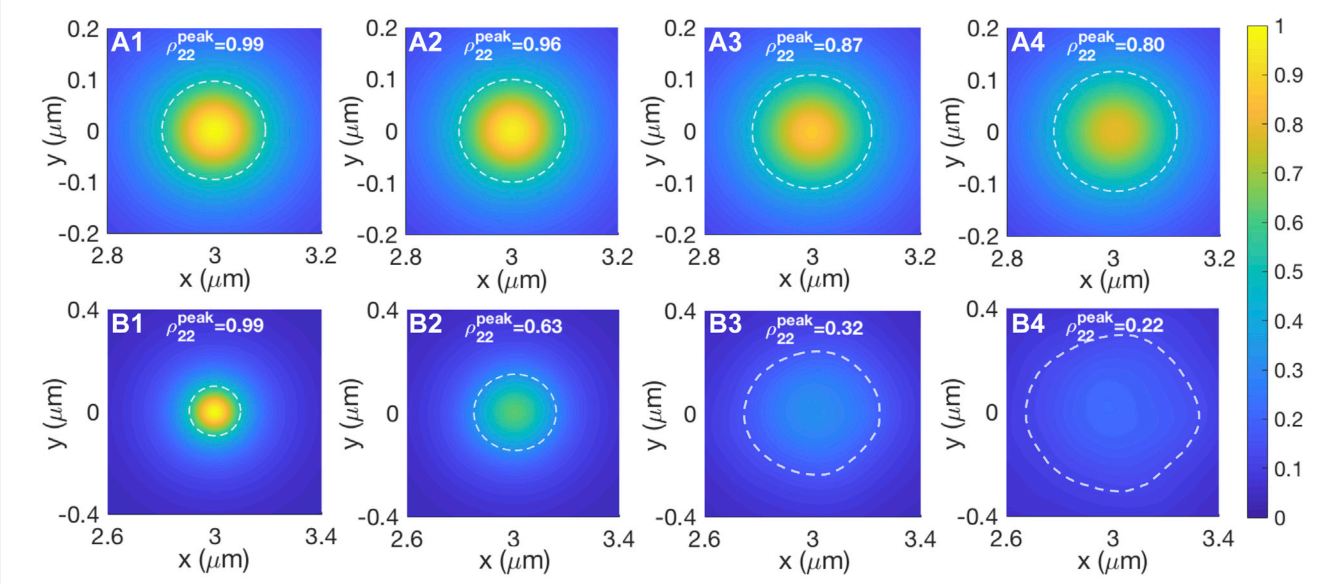

FIGURE 6 | (A1–A4) 2D population distribution of $\rho_{22}(r)$ under different temperatures T = (0, 1, 5, 10)μK. The peak value of $\rho_{22}(r)$ is given in the picture and the diameter of white-dashed rings stands for the spatial resolution a_r, which is a_r = (200, 206, 222, 247) nm, respectively. Here, we assume the measurement time is T_{meas} = 1 μs. Analogous to **(A1–A4)**, **(B1–B4)** show the case of T_{meas} = 5 μs and the calculated resolution is a_r = (200, 308, 530, 687) nm. Every point is obtained by averaging over 500 measurements.

(300 nm) can be obtained within a localized radius of $r_{loc} < 3.7\ \mu$m (5.3 μm), see the insets of **Figures 5A,B** for a more visible representation. In addition, since the steady time is inversely proportional to the exact Rabi frequencies the limitation for a best off-axis localization can further be overcome by a stronger coupling laser. For example, when $\Omega_{c10}/2\pi$ = 300 MHz and $\Omega_{p0}/2\pi$ = 2.7 MHz the best spatial resolution of our protocol can be reduced to 91 nm if atoms are localized in the beam core (not shown).

5.3 Noise From Atomic Thermal Motion

In a real experimental setup due to atomic thermal motion, the laser intensity 'seen' by atoms would have a strong perturbation, which intuitively brings a noise on detecting the steady atomic population. Here, we consider atoms move randomly in space whose velocities satisfy a two-dimensional Maxwell–Boltzmann distribution [45].

$$f\left(v_x, v_y\right) = \frac{1}{\pi v_p^2} e^{-\left(v_x^2+v_y^2\right)/v_p^2}. \tag{13}$$

Here, v_p is the most probable velocity defined by $v_p = \sqrt{2k_B T/M}$. Other interatomic collisions are ignored. During the jth measurement we assume a simple uniform motion of atoms by letting

$$\left(x_j, y_j\right) \to \left(x_j + v_x T_{meas}, y_j + v_y T_{meas}\right), \tag{14}$$

where (v_x, v_y) are obtained stochastically from the velocity function $f\ (v_x, v_y)$ and T_{meas} is the time for single measurement. By inserting **Eq. 14** into **Eqs 1**, **2** atoms can feel a fluctuated Rabi frequency $\Omega_i(t)$ ($i = p, c1, c2$) for each measurement. The final results are based on an average of 500 times random samplings of the velocity (v_x, v_y).

In **Figure 6**, we show the calculated population distribution $\rho_{22}(r)$ under sufficient measurements in the x–y frame. Clearly, from **Figures 6A1–A4** due to a larger probable velocity of atoms caused by the growing temperature, the peak value ρ_{22}^{peak} has an explicit decrease together with a lower spatial resolution a_r. For example, when $T = 1\ \mu K$, a_r = 206 nm which is close to the value at T = 0. Because the average distance of atoms during each measurement (T_{meas} = 1 μs) is only $v_p T_{meas} \approx 14$ nm, which is much smaller than a_r. However, as for a higher temperature the movement of atoms during each measurement can cause a bigger effect making the precision of atom localization worse. See the case of $T = 10\ \mu K$ in **Figure 6A4**, we observe that ρ_{22}^{peak} = 0.8 and a_r = 247 nm. For comparison in **Figures 6B1–B4** we also study the case of a longer measurement time (T_{meas} = 5 μs) where atoms can move farther, leading to a very poor spatial resolution at a finite temperature. We numerically show that at $T = 10\ \mu K$ the distribution of atomic population $\rho_{22}(r)$ has become slightly deformed with its peak value (spatial resolution) as low as ρ_{22}^{peak} = 0.22(a_r = 687 nm). That fact means such a long-time measurement has made most atoms away from the localization spot *via* their thermal movements. Therefore a faster measurement accompanied by a lower environment temperature can facilitate high-quality atom localization.

6 CONCLUSION

To conclude, our scheme presents a novel 2D atom localization, having both ultraprecise and off-axis features.

Differing from the previous works using a single LG field we adopt a LG beam together with a Gaussian beam as the hybrid coupling field. The previous contributions can only localize atom in the beam core where the intensity of coupling field is zero. While our protocol shows that atoms can be localized at arbitrary position due to the effect of quantum interference between these two coupling beams that leads to a zero-intensity spot in space. Our numerical simulation confirms that with an appropriate adjustment for the peak ratios of laser Rabi frequencies a wider off-axis localization range and higher quality spatial resolution can be achieved at the same time. Under experimentally feasible parameters an estimation for the implementation of realistic off-axis atom localization is predicted, promising for a resolution of ~ 200 nm and a localized radius of a few μm. In addition, we also discuss the weakness of our scheme when some intrinsic quantum noises from imperfect measurement, including laser intensity noise, limited steady time, and atomic thermal motion, are considered. Our approach may provide unique application to atomic lithography with more flexibility and better resolution [46]. An extension to the 3D off-axis atom localization is possible by implementing a spatial modulation to the probe detuning which is our next-step work [32].

DATA AVAILABILITY STATEMENT

The original contributions presented in the study are included in the article/Supplementary Material; further inquiries can be directed to the corresponding author.

AUTHOR CONTRIBUTIONS

The idea was first conceived by NJ. NJ was responsible for the physical modeling, the numerical calculations, and writing the original draft under the supervision of JQ. JQ contributed to review and editing. JQ verified results of the theoretical calculation. X-DZ contributed to editing the draft. X-DZ and W-RQ contributed to the discussion of the results.

FUNDING

This work was supported by the National Natural Science Foundation of China under Grant Nos 12104308, 12174106, 11474094, 11104076, 12104135, and 11604086; by the Science and Technology Commission of Shanghai Municipality under Grant No. 18ZR1412800.

REFERENCES

1. Babiker M, Andrews DL, Lembessis VE. Atoms in Complex Twisted Light. *J Opt* (2018) 21:013001. doi:10.1088/2040-8986/aaed14
2. Grier DG. A Revolution in Optical Manipulation. *Nature* (2003) 424:810–6. doi:10.1038/nature01935
3. Padgett M, Bowman R. Tweezers with a Twist. *Nat Photon* (2011) 5:343–8. doi:10.1038/nphoton.2011.81
4. Ran L-L, Guo Z-Y, Qu S-L. Rotational Motions of Optically Trapped Microscopic Particles by a Vortex Femtosecond Laser. *Chin Phys. B* (2012) 21:104206. doi:10.1088/1674-1056/21/10/104206
5. Dholakia K, Simpson NB, Padgett MJ, Allen L. Second-Harmonic Generation and the Orbital Angular Momentum of Light. *Phys Rev A* (1996) 54: R3742–R3745. doi:10.1103/PhysRevA.54.R3742
6. Kong F, Zhang C, Bouchard F, Li Z, Brown GG, Ko DH, et al. Controlling the Orbital Angular Momentum of High Harmonic Vortices. *Nat Commun* (2017) 8:14970. doi:10.1038/ncomms14970
7. Gauthier D, Ribič PR, Adhikary G, Camper A, Chappuis C, Cucini R, et al. Tunable Orbital Angular Momentum in High-Harmonic Generation. *Nat Commun* (2017) 8:14971. doi:10.1038/ncomms14971
8. Vicidomini G, Bianchini P, Diaspro A. Sted Super-Resolved Microscopy. *Nat Methods* (2018) 15:173–82. doi:10.1038/nmeth.4593
9. Schermelleh L, Ferrand A, Huser T, Eggeling C, Sauer M, Biehlmaier O, et al. Super-Resolution Microscopy Demystified. *Nat Cell Biol* (2019) 21:72–84. doi:10.1038/s41556-018-0251-8
10. Masullo LA, Steiner F, Zähringer J, Lopez LF, Bohlen J, Richter L, et al. Pulsed Interleaved Minflux. *Nano Lett* (2021) 21:840–6. doi:10.1021/acs.nanolett.0c04600
11. Balzarotti F, Eilers Y, Gwosch KC, Gynnå AH, Westphal V, Stefani FD, et al. Nanometer Resolution Imaging and Tracking of Fluorescent Molecules with Minimal Photon Fluxes. *Science* (2017) 355:606–12. doi:10.1126/science.aak9913
12. Proite NA, Simmons ZJ, Yavuz DD. Observation of Atomic Localization Using Electromagnetically Induced Transparency. *Phys Rev A* (2011) 83:041803. doi:10.1103/PhysRevA.83.041803
13. Miles JA, Simmons ZJ, Yavuz DD. Subwavelength Localization of Atomic Excitation Using Electromagnetically Induced Transparency. *Phys Rev X* (2013) 3:031014. doi:10.1103/PhysRevX.3.031014
14. Miles JA, Das D, Simmons ZJ, Yavuz DD. Localization of Atomic Excitation Beyond the Diffraction Limit Using Electromagnetically Induced Transparency. *Phys Rev A* (2015) 92:033838. doi:10.1103/PhysRevA.92.033838
15. Qamar S, Zhu S-Y, Zubairy MS. Precision Localization of Single Atom Using Autler-Townes Microscopy. *Opt Commun* (2000) 176:409–16. doi:10.1016/S0030-4018(00)00535-6
16. Ghafoor F, Qamar S, Zubairy MS. Atom Localization via Phase and Amplitude Control of the Driving Field. *Phys Rev A* (2002) 65:043819. doi:10.1103/PhysRevA.65.043819
17. Ghafoor F. Subwavelength Atom Localization via Quantum Coherence in a Three-Level Atomic System. *Phys Rev A* (2011) 84:063849. doi:10.1103/PhysRevA.84.063849
18. Wan R-G, Zhang T-Y. Two-Dimensional Sub-Half-Wavelength Atom Localization via Controlled Spontaneous Emission. *Opt Express* (2011) 19: 25823–32. doi:10.1364/OE.19.025823
19. Yavuz DD, Proite NA. Nanoscale Resolution Fluorescence Microscopy Using Electromagnetically Induced Transparency. *Phys Rev A* (2007) 76:041802. doi:10.1103/PhysRevA.76.041802
20. Paspalakis E, Knight PL. Localizing an Atom via Quantum Interference. *Phys Rev A* (2001) 63:065802. doi:10.1103/physreva.63.065802
21. Kapale KT, Agarwal GS. Subwavelength Atom Localization via Coherent Population Trapping. In: Frontiers in Optics (Optica Publishing Group) (2006). p. FThO5. doi:10.1364/FIO.2006.FThO5
22. Ivanov V, Rozhdestvensky Y. Two-Dimensional Atom Localization in a Four-Level Tripod System in Laser Fields. *Phys Rev A* (2010) 81:033809. doi:10.1103/PhysRevA.81.033809
23. Ivanov VS, Rozhdestvensky YV, Suominen K-A. Three-Dimensional Atom Localization by Laser Fields in a Four-Level Tripod System. *Phys Rev A* (2014) 90:063802. doi:10.1103/PhysRevA.90.063802
24. Wang Z, Yu B. High-Precision Two-Dimensional Atom Localization via Quantum Interference in a Tripod-Type System. *Laser Phys Lett* (2014) 11: 035201. doi:10.1088/1612-2011/11/3/035201
25. Zhu Z, Yang W-X, Chen A-X, Liu S, Lee R-K. Dressed-State Analysis of Efficient Three-Dimensional Atom Localization in a Ladder-Type Three-Level Atomic System. *Laser Phys* (2016) 26:075203. doi:10.1088/1054-660x/26/7/075203

26. Sahrai M, Tajalli H, Kapale KT, Zubairy MS. Subwavelength Atom Localization via Amplitude and Phase Control of the Absorption Spectrum. *Phys Rev A* (2005) 72:013820. doi:10.1103/PhysRevA.72.013820
27. Sahrai M, Mahmoudi M, Kheradmand R. Atom Localization of a Two-Level Pump-Probe System via the Absorption Spectrum. *Laser Phys* (2007) 17:40–4. doi:10.1134/S1054660X07010082
28. Zhang D, Yu R, Sun Z, Ding C, Zubairy MS. Efficient Three-Dimensional Atom Localization Using Probe Absorption in a Diamond-Configuration Atomic System. *J Phys B: Mol Opt Phys* (2019) 52:035502. doi:10.1088/1361-6455/aaf5ec
29. Qamar S, Mehmood A, Qamar S. Subwavelength Atom Localization via Coherent Manipulation of the Raman Gain Process. *Phys Rev A* (2009) 79: 033848. doi:10.1103/PhysRevA.79.033848
30. Wan R-G, Zhang T-Y, Kou J. Two-Dimensional Sub-Half-Wavelength Atom Localization via Phase Control of Absorption and Gain. *Phys Rev A* (2013) 87: 043816. doi:10.1103/PhysRevA.87.043816
31. Kazemi SH, Veisi M, Mahmoudi M. Atom Localization Using Laguerre-Gaussian Beams. *J Opt* (2019) 21:025401. doi:10.1088/2040-8986/aafe61
32. Jia N, Qian J, Kirova T, Juzeliūnas G, Reza Hamedi H. Ultraprecise Rydberg Atomic Localization Using Optical Vortices. *Opt Express* (2020) 28:36936–52. doi:10.1364/OE.411130
33. Ding C, Li J, Yang X, Zhang D, Xiong H. Proposal for Efficient Two-Dimensional Atom Localization Using Probe Absorption in a Microwave-Driven Four-Level Atomic System. *Phys Rev A* (2011) 84:043840. doi:10.1103/PhysRevA.84.043840
34. Hamedi HR, Juzeliūnas G. Phase-Sensitive Atom Localization for Closed-Loop Quantum Systems. *Phys Rev A* (2016) 94:013842. doi:10.1103/PhysRevA.94.013842
35. Rahmatullah U, Qamar S. Two-Dimensional Atom Localization via Probe-Absorption Spectrum. *Phys Rev A* (2013) 88:013846. doi:10.1103/PhysRevA.88.013846
36. Hong Y, Wang Z, Yu B. High-Precision Three-Dimensional Atom Localization via Kerr Nonlinearity. *J Opt Soc Am B* (2019) 36:746–51. doi:10.1364/JOSAB.36.000746
37. Franke-Arnold S, Leach J, Padgett MJ, Lembessis VE, Ellinas D, Wright AJ, et al. Optical Ferris Wheel for Ultracold Atoms. *Opt Express* (2007) 15: 8619–25. doi:10.1364/OE.15.008619
38. Hamedi HR, Paspalakis E, Žlabys G, Juzeliūnas G, Ruseckas J. Complete Energy Conversion Between Light Beams Carrying Orbital Angular Momentum Using Coherent Population Trapping for a Coherently Driven Double- Λ Atom-Light-Coupling Scheme. *Phys Rev A* (2019) 100:023811. doi:10.1103/PhysRevA.100.023811
39. Wang Z, Yu B. Efficient Three-Dimensional Atom Localization via Probe Absorption. *J Opt Soc Am B* (2015) 32:1281–6. doi:10.1364/JOSAB.32.001281
40. Paspalakis E, Terzis AF, Knight PL. Quantum Interference Induced Sub-Wavelength Atomic Localization. *J Mod Opt* (2005) 52:1685–94. doi:10.1080/09500340500072489
41. Qiu J, Wang Z, Yu B. Generation of New Structured Beams via Spatially Dependent Transparency. *Quan Inf Process* (2019) 18:160. doi:10.1007/s11128-019-2278-6
42. Volz U, Schmoranzer H. Precision Lifetime Measurements on Alkali Atoms and on Helium by Beam-Gas-Laser Spectroscopy. *Phys Scr* (1996) T65:48–56. doi:10.1088/0031-8949/1996/t65/007
43. Dridi G, Guérin S, Hakobyan V, Jauslin HR, Eleuch H. Ultrafast Stimulated Raman Parallel Adiabatic Passage by Shaped Pulses. *Phys Rev A* (2009) 80: 043408. doi:10.1103/PhysRevA.80.043408
44. Kang Y-H, Chen Y-H, Shi Z-C, Huang B-H, Song J, Xia Y. Nonadiabatic Holonomic Quantum Computation Using Rydberg Blockade. *Phys Rev A* (2018) 97:042336. doi:10.1103/PhysRevA.97.042336
45. Huo X, Chen JF, Qian J, Zhang W. Interaction-Enhanced Transmission Imaging with Rydberg Atoms. *Phys Rev A* (2022) 105:012817. doi:10.1103/PhysRevA.105.012817
46. Johnson KS, Thywissen JH, Dekker NH, Berggren KK, Chu AP, Younkin R, et al. Localization of Metastable Atom Beams with Optical Standing Waves: Nanolithography at the Heisenberg Limit. *Science* (1998) 280:1583–6. doi:10.1126/science.280.5369.1583

Conflict of Interest: The authors declare that the research was conducted in the absence of any commercial or financial relationships that could be construed as a potential conflict of interest.

Publisher's Note: All claims expressed in this article are solely those of the authors and do not necessarily represent those of their affiliated organizations, or those of the publisher, the editors, and the reviewers. Any product that may be evaluated in this article, or claim that may be made by its manufacturer, is not guaranteed or endorsed by the publisher.